CONFERENCE PRE-PRINT

PROGRESS OF CORE-EDGE INTEGRATED TUNGSTEN TRANSPORT STUDY IN EAST WITH ITER-LIKE TUNGSTEN DIVERTORS USING ADVANCED IMPURITY DIAGNOSTICS

L. ZHANG1

¹Institute of Plasma Physics, Chinese Academy of Sciences, Hefei, China

Email: zhangling@ipp.ac.cn

S. MORITA^{1,2}, C.X. ZHOU¹, Y.X. CHENG¹, W.M. ZHANG^{1,3}, P. MANAS⁴, D. MITNIK⁵, T. FONGHETTI⁴, A.L. HU¹, Q.Q. YANG¹, Z. ZHOU^{1,3}, R.J. BAO^{1,3}, J.H. Chen¹, S.X. WANG¹, Y.W. SUN¹, J.P. QIAN¹, X.Z. GONG¹, X. GAO¹, H.Q. LIU¹, Y.T. SONG¹

²National Institute for Fusion Science, Toki, Japan

³University of Science and Technology of China, Hefei, China

⁴CEA, IRFM, F-13108 Saint Paul-lez-Durance, France

⁵Instituto de Astronomía y Física del Espacio, Buenos Aires, Argentina

Abstract

ITER has selected tungsten (W) as the plasma-facing material. High-Z W impurities entering the plasma core degrade plasma confinement through enhanced radiation power. Understanding W transport across operational regimes and regulating impurity accumulation is therefore critical. On EAST, dedicated experiments combined with modeling are used to study W transport in the main confinement region for hybrid and fully non-inductive operation and identify the dominant mechanisms. Based on these mechanisms, effective control routes are identified, including on-axis ECRH, LHW, ICRH, and 3D RMPs. In NBI-dominated H-mode plasmas, the ELM type determines core tungsten concentrations (Cw). Discharges exhibiting type-III ELMs maintain Cw between 5.6×10^{-6} and 6.3×10^{-5} , while type-I ELM discharges show higher Cw ranging from 5.7×10^{-5} to 2.0×10^{-4} . Analysis of type-I ELMs reveals two distinct cases, i.e., with and without impurity sputtering events. Without impurity sputtering, W and Mo content in the main confinement region oscillate between intra-ELM depletion and inter-ELM recovery due to SOL backflow, maintaining near-constant time-averaged levels. When sputtering occurs, impurities from both high-field and low-field sides penetrate into the plasma core during inter-ELM phases, increasing radiation power and degrading plasma confinement until subsequent ELM bursts effectively remove them. Increasing ELM frequency enhances impurity expulsion during intra-ELM while suppressing inter-ELM backflow, providing an effective control mechanism for core impurity accumulation.

1. INTRODUCTION

International Thermonuclear Experimental Reactor (ITER) will operate with all-tungsten plasma-facing components (PFCs), following the updated baseline that replaces beryllium with tungsten (W) as the first wall material [1]. Impurities significantly affect high-performance plasmas in magnetic confinement fusion, as radiation power loss and bulk ion dilution caused by impurity ions can rapidly degrade plasma performance. Radiation loss is well known to scale strongly with the atomic number (Z) of the impurity element. Experimental Advanced Superconducting Tokamak (EAST) has been equipped with upper and lower tungsten (W) divertors since 2014 and 2021, respectively. Therefore, the impact on plasma performance in its steady-state operation must be studied in detail as the highest priority issue in EAST in addition to the study of W transport. For this purpose, a complete set of tungsten spectroscopy diagnostic systems has been developed and installed on EAST, which consists of a visible (VIS) spectroscopy system [2, 3], fast-time-response [4, 5], and space-resolved extreme ultraviolet (EUV) spectroscopy systems [6, 7]. Fast-time-response EUV spectroscopy system includes four grazing-incidence flat-field spectrometers developed on EAST since 2014. One is working at 5-138 Å [5], and the other three are working at 20-500 Å [4]. EUV spectra with high spectral resolution at the full range of 5-500 Å could be observed simultaneously in each discharge at a sampling rate of 5 ms/frame. More than eight hundred emission lines from low-Z and high-Z impurity ions have been carefully identified from the EUV spectra as a fundamental work. Moreover, a database of EUV lines from multiple impurity elements in fusion plasma has been preliminarily built [8-10]. Based on this

database, machine learning has been applied to the wavelength calibration for EUV spectroscopy in EAST [11]. Space-resolved EUV spectroscopy system also includes four spectrometers [7], which have been installed successively since 2017. Two of them working at 5-138 Å provide the tungsten line intensity profiles in p≤0.3 with 15-50 ms/frame, and the other two working at 30-520 Å provide that in p≤0.7 with 50-200 ms/frame. Meanwhile, an integrated NEO+TGLF+STRAHL modelling for the simulation study on core W transport has been also developed under OMFIT framework [12]. The W transport characteristics at plasma core in hybrid [13] and fully non-inductive [14] discharge scenarios are explored by combining simulation and experimental studies. It was found that in EAST under hybrid discharges, the strong toroidal rotation and peaked bulk plasma density synergistically drive a significant neoclassical inward pinch of W, leading to W impurity accumulation [13]. In contrast, in improved high-performance fully non-inductive discharge, the electron temperature (T_e) and its gradient are typically high, while the bulk plasma exhibits small toroidal rotation and weak density peaking. Here, the W turbulent diffusion coefficient is sufficiently large to offset the combined turbulent and neoclassical pinch, such that the W density profile remains weakly peaked under zero particle flux, suppressing impurity accumulation [14]. As a result, on-axis electron cyclotron resonance heating (ECRH) [14], 4.6GHz lower hybrid wave (LHW) [15] and ion cyclotron resonance heating (ICRH) [16] heating have proved to be effective to control the core W ions through enhanced radial transport. Specifically, ECRH and LHW both increase W turbulent diffusion by elevating the electron temperature and its gradient. LHW further mitigate neoclassical inward pinch by reducing toroidal rotation (V_t), a mechanism shared with ICRH. In addition, up/down poloidal asymmetry was observed for W ions in EAST for the first time. The V_t was found to play an essential role in enhancing the asymmetry. A strong asymmetric distribution was also found for ions existing in peripheral region.

Based on the simulation study, turbulent W transport is predicted to be dominant over the neoclassical transport in plasma core region of conventional H-mode discharges in both ITER [17] and CFEDR [18] next-generation tokamaks. A more important point, however, is the control of W ions in the edge pedestal region. Unfortunately, the study on pedestal tungsten transport remained insufficient due to a lack of the line observation for weakly and moderately ionized W ions and the absence of transport modelling for the pedestal region. Recently, weekly and moderately ionized W⁴⁺-W²⁰⁺ ions existing in the SOL-pedestal-edge regions including other metallic impurity ions have been observed and identified [8, 9] in the EAST plasma with edge-performance improved spectroscopy diagnostics. Benefiting from the observation, a diagnostic gap between divertor W source and core W behavior, i.e., a spectral gap between W atom and highly ionized W ions of W²⁴⁺-W⁴⁵⁺, can be adequately filled. A collision-radiative (CR) model has been built for such weekly ionized W ions, e.g. W⁵⁺-W⁷⁺, to calculate the photon ionization event (S/XB) for W influx evaluation [19]. Based on this model, the S/XB coefficients of weakly ionized states of other impurity ions on the EAST were calculated. Combined with the evolution characteristics of impurity ion influx, a study was carried out to investigate the effect of the edge impurity screening layer induced by resonant magnetic perturbations (RMPs) on impurity transport in the SOL-edge-core region [20, 21]. The position and width of the screening layer could be roughly estimated through the evolution characteristics of impurity ion influx combined with T_c . Furthermore, It was found that the formation of the impurity screening layer not only effectively reduced the impurity ion concentration in the main confinement region but also indirectly improved plasma confinement performance by weakening the neoclassical inward pinch through the reduction of electron density peaking and toroidal rotation and by enhancing turbulent diffusion through the increase of electron temperature and its gradient, ultimately suppressing impurity accumulation effectively. Currently, a universal approach to calculate on the photon emissivity coefficient (PEC) of high-Z impurity ions with multiple ionization stages is being under development, which will contribute to significantly enhancing the ADAS database. Using this approach, PECs of molybdenum (Mo) and W ions across multiple ionization stages were obtained, and based on these PECs, the density profiles of Mo and W impurities in internal transport barrier (ITB) discharges were investigated [22]. Significant differences in impurity transport exist between the regions inside and outside the ITB, where the impurity density distribution from the ITB foot to the scrape-off layer (SOL) remains stable, while impurity behavior from the magnetic axis to the ITB foot varies significantly with ITB type. In ion temperature ITB (T_i-ITB), the ion temperature screening effect dominates and effectively suppresses impurity accumulation, whereas in electron density ITB (ne-ITB), the enhanced electron density gradient drives impurity accumulation.

In natural ELM-free discharges and discharges with ELMs suppressed by radio frequency (RF) wave heating, damage to plasma-facing components (PFCs) caused by high transient heat and particle fluxes can be effectively avoided. However, impurity accumulation degrades overall performance, which is

detrimental to sustaining long-pulse steady-state high-confinement plasma. Therefore, balancing ELM-induced heat flux mitigation against impurity accumulation is critical for the operation of fusion devices. Very recently, considering the PFCs configuration of EAST with Mo first wall and W divertor, core-edge integrated Mo and W behavior study started to be carried out for H-mode discharges under distinct ELM activity regime particularly using Mo and W impurity sputtering events.

2. EXPERIMENTAL RESULTA AND DISCUSSION

Tungsten impurity accumulation and strong radiation loss in the plasma core are frequently observed in neutral beam injection (NBI)-dominated discharges on EAST. Simultaneously, as the discharges duration increases, the tungsten impurity concentration (C_W) in the plasma core continues to increase. These effects are particularly pronounced during type-I ELM discharges. Fig. 1 presents the dependence of W concentration on ELM frequency (f_{ELM}) for discharges with plasma currents of 350-550 kA, where the C_W is evaluated with a combination of intensities of the W unresolved transition array (W-UTA: W²⁴⁺-W⁴⁵⁺) in 45-70 Å measured by fast-time-response EUV spectrometer (EUV Long a) and total radiation loss. The results show that the tungsten impurity concentration in pure type-I ELM discharges (f_{ELM}=10-100 Hz) is significantly higher than that in pure type-III ELM discharges (f_{ELM}=100-600 Hz), where C_W ranges from 5.7×10⁻⁵ to 2.0×10⁻⁴ for type-I ELMs and from 5.6×10⁻⁶ to 6.3×10⁻⁵ for type-III ELMs. However, previous experiments result on EAST indicated that H-L transitions and plasma disruptions are highly probable when the C_W falls within the range of 6.0×10⁻⁵<C_W<3.0×10⁻⁴. In addition, as shown in Fig. 1, when type-III ELMs emerge during the inter-ELM phase of type-I ELM discharges, the C_W can decrease to a level comparable to that in pure type-III ELM discharges. It is noted that the tolerance limit for tungsten impurity concentration in the pedestal top is on the order of 10⁻⁵ in ECRH-heated ITER plasmas [23].

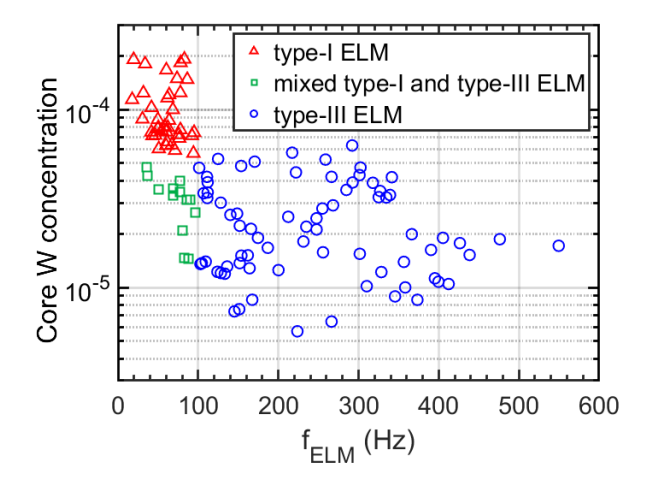


Fig. 1. Tungsten concentration in plasma core, Cw, as function of ELM frequency, felm, in EAST NBI-dominant heating H-mode discharges. Red solid triangles, green square, and blue solid circles denote type-I ELM, mixed type-III ELM discharges, respectively.

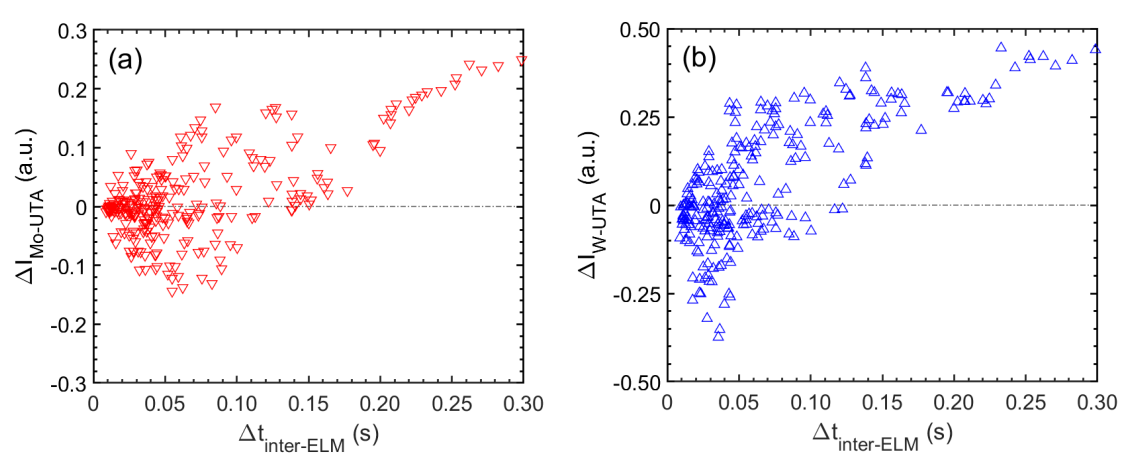


Fig. 2. Dependence of impurity intensity variations, ΔI_{imp} , against pure type-I ELM intermission interval, $\Delta I_{imter-ELM}$: (a) molybdenum intensity variation, ΔI_{MO-UTA} , and (b) tungsten intensity variation, ΔI_{W-UTA} .

Experimental results from fusion devices indicate that the tungsten screening effect of the divertor can be very efficient, and the tungsten influx at the divertor is not necessarily the one that impacts the most the tungsten content in the confined plasmas in the presence of a full tungsten wall. Moreover, while the tungsten influx generated at the low-field side is the lowest, its influence on the tungsten concentration in the plasma core is more significant. For this reason, the statistical analysis of Mo impurity from the first wall and W impurity from the divertor during the inter-ELM interval ($\Delta t_{inter-ELM}$) of type-I ELM on EAST is performed, as shown in Fig. 2. The data are selected from pure type-I ELM discharges, excluding transient impurity sputtering and core magnetohydrodynamic (MHD) events. The Mo-UTA emission in Fig. 2(a) primarily originates from Mo²²⁺-Mo²⁹⁺ at 70–95 Å. For $\Delta t_{inter-ELM}$ >0.15 s (f_{ELM} <7 Hz), core Mo and W intensities variation (Δt_{Mo-UTA} and Δt_{W-UTA}) increase monotonically with interval duration. However, for $\Delta t_{inter-ELM}$ <0.15 s (f_{ELM} >7 Hz), both Δt_{Mo-UTA} and Δt_{W-UTA} exhibit non-monotonic evolution. When $\Delta t_{inter-ELM}$ <0.06 s, the W-UTA intensity reduction (Δt_{W-UTA} <0) primarily results from ELM-induced impurity expulsion. Therefore, W and Mo impurity behavior is studied in a representative pure type-I ELM discharge with t_{ELM} <0.10 Hz.

Fig. 3 illustrates a natural type-I ELM discharge (shot #152527, Ip=0.45 MA, B_t=-2.4 T, T_{e0}=1.8 keV, n_e =4.9×10¹⁹ m⁻³) under steady heating (P_{ECRH} =1.35 MW, P_{NBI} =1.2 MW). The D_a signal (Fig. 3(a)) reveals non-uniform ELM frequency and amplitude. Each ELM burst causes abrupt drops in ne and W_{MHD} due to pedestal collapse (see Figs. 3(b) and 3(c)), followed by rapid recovery during inter-ELM intervals. The lines-of-sights (LOS) of edge AXUV and SXR (Figs. 3(d) and 3(e)) mainly observes the SOL and pedestal region, respectively. A 12.5 µm thin film covering the SXR collimator restricts the photon energy response to 1-15 keV, which explains why no spike signals similar to those in D_{α} and edge AXUV appear in edge SXR. On the other hand, in this discharge, other high-Z impurities (i.e., Fe, Cu) exhibit significantly lower concentrations than W and Mo, leading to negligible radiative contributions. Therefore, variation in core I_{SXR} better reflects Mo impurity behavior, while core I_{AXUV} more clearly characterizes W impurities in EAST, due to their different detection ranges. As shown in Fig. 3(d) and 3(e), during t=6.0-8.5 s, the core I_{AXUV} and I_{SXR} show exclusively opposite trends between 7.379-7.576 s (I_{AXUV} significantly increases, I_{SXR} decreases). Concurrently, edge I_{AXUV} and I_{SXR} exhibit small increases during t=7.379-7.418 s, suggesting W impurity likely bursts and penetrates the plasma core. This results in significant radiation losses and W_{MHD} degradation until ELM expulsion enables recovery (see Fig. 3(c)). In addition, at t=7.829 s, the edge AXUV signal shows a transient radiation increase (green-shaded area). This event leads to significant increases in core and edge SXR radiation at t=7.829-7.975s that implicate Mo as the dominant sputtering impurity. A comprehensive analysis of W and Mo impurity dynamics during t=6.0–8.5 s will be presented subsequently.

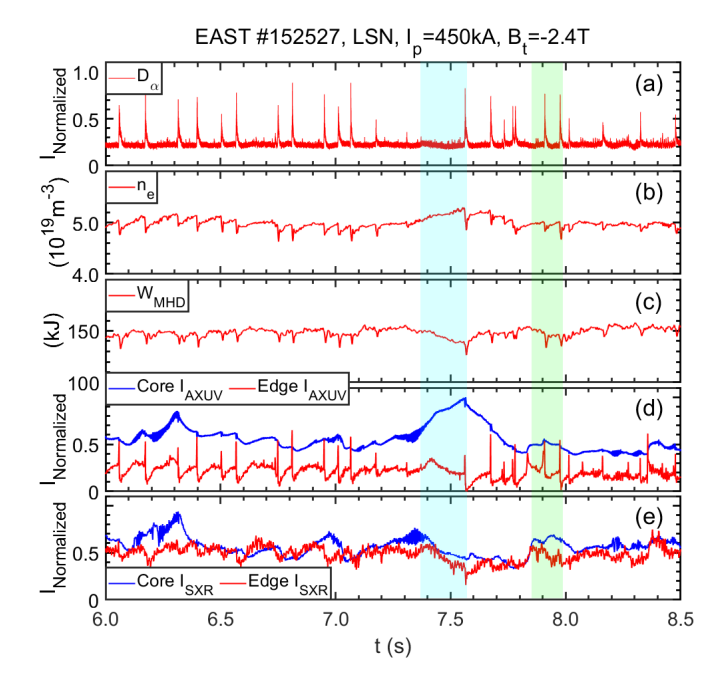
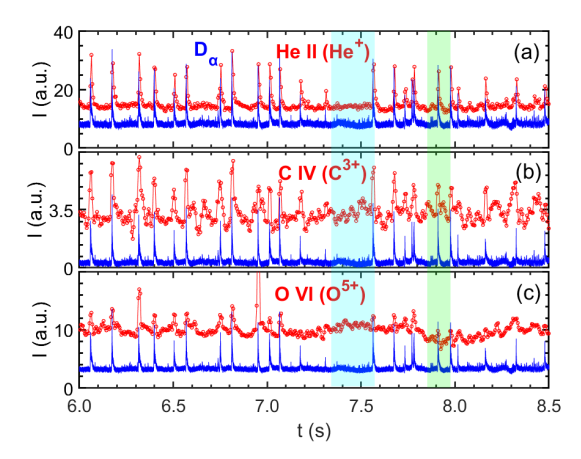


Fig. 3. Typical waveform of natural type-I ELM discharge with tungsten and molybdenum impurity sputtering during plasma current flat top: (a) normalized D_{α} intensity of lower divertor, (b) line-averaged electron density, $n_{\rm e}$, (c) plasma stored energy, $W_{\rm MHD}$, (d) normalized Core $I_{\rm AXUV}$ and Edge $I_{\rm AXUV}$ radiation power, and (e) normalized Core $I_{\rm SXR}$ and Edge $I_{\rm SXR}$. Cyan-shaded (t=7.368-7.567 s) and green-shaded areas (t=7.856-7.993 s) indicate significant increase in core AXUV and SXR, respectively.

During the discharge #152527, the fast-response spectrometers of EUV_Long_a, EUV_Long_c, and EUV_Long_b operate in the wavelength ranges of 20-150 Å, 130-330 Å, and 270-480 Å, respectively.

Meanwhile, the space-resolved EUV_Long2_u spectrometer operates in the wavelength range of 45-75 Å, primarily used to measure the intensity distribution of W and Mo impurity ions. The evolution of low-Z impurity ions in EAST is shown in Fig. 4. The evolution characteristics of these impurity ions indicate that He⁺ at 303.780 Å and C³⁺ at 384.180 Å are primarily confined to the SOL region, where the increase in impurity emission is generally proportional to the strength of ELM events during the intra-ELM phase. In contrast, O⁵⁺ ions at 173.095 Å are mainly concentrated in the pedestal, in which no significant correlation is observed between intensity variations and the strength of the ELM bursts.



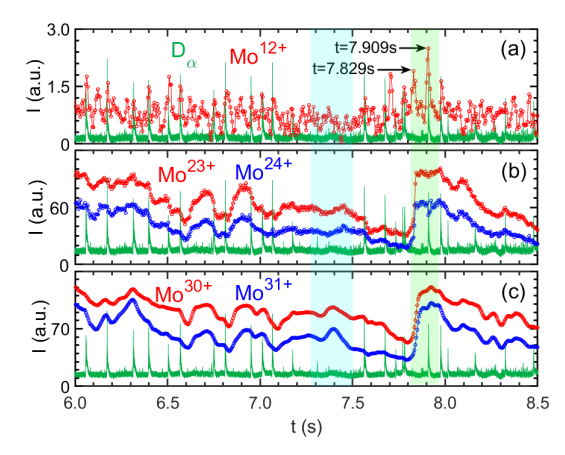


Fig. 4. Time evolutions of low-Z impurities at the SOL and pedestal: (a) He II at 303.780 Å, (b) C IV at 384.180 Å, and (c) O VI at 173.095 Å. The two shaded areas are defined in Fig. 3.

Fig. 5. Time evolutions of molybdenum impurity ions from pedestal to plasma core: (a) Mo^{12+} at 340.909 Å, (b) Mo^{23+} at 71.175 Å and Mo^{24+} at 74.170 Å, and (c) Mo^{30+} at 115.999 Å and Mo^{31+} at 127.868 Å. The two shaded areas are defined in Fig. 3.

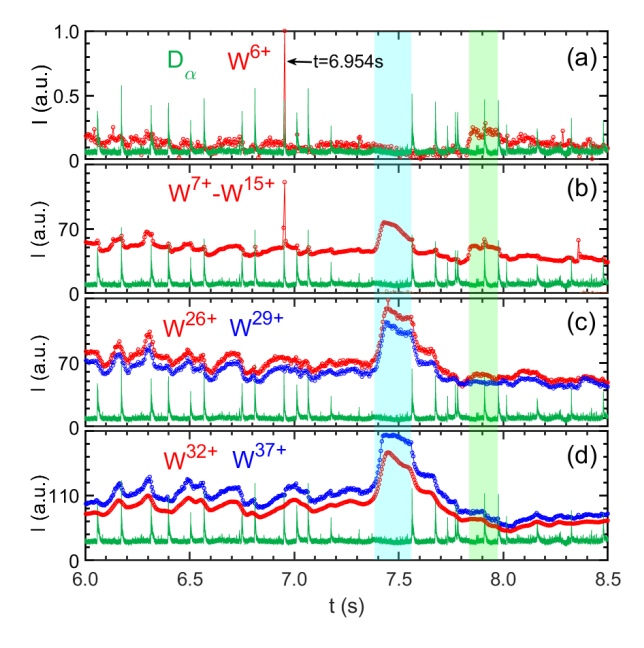


Fig. 6. Time evolutions of tungsten impurity ions from SOL to plasma core: (a) W^{6+} at 216.219 Å, (b) W^{7+} - W^{15+} at 160-220 Å, (c) W^{26+} at 49.0 Å and W^{29+} at 49.938 Å, and (d) W^{32+} at 52.20 Å and W^{37+} at 56.880 Å. The two shaded areas are defined in Fig. 3.

The evolution of high-Z impurity Mo and W ions is shown in Figs. 5 and 6. Based on previous studies, Mo¹²⁺ at 340.909 Å and Mo²³⁺-Mo³¹⁺ ions (Mo²³⁺ at 71.175 Å, Mo²⁴⁺ at 74.170 Å, Mo³⁰⁺ at 115.999 Å, Mo³¹⁺ at 127.868 Å) are located in the pedestal and main confinement region, respectively. W⁶⁺ at 216.219 Å is found from the SOL to the foot of the pedestal, while the lowly ionized states W-UTA from W⁷⁺-W¹⁵⁺ at 170-220 Å are primarily in the pedestal to the edge region, and W²⁶⁺-W³⁷⁺ ions (W²⁶⁺ at 49.0 Å, W²⁹⁺ at 49.938 Å, W³²⁺ at 52.20 Å, W³⁷⁺ at 56.880 Å) are located in the main confinement region. Notably, Mo¹²⁺ ions are the lowest ionization state of Mo suitable for impurity transport studies in #152527 discharge. As shown in Fig. 5, the intensity of Mo¹²⁺ increases sharply during the intra-ELM phase, while Mo²³⁺-Mo³¹⁺ ions decrease rapidly. During the inter-ELM phase, the emission of Mo¹²⁺ continues to decrease. However, the emission of Mo²³⁺-Mo³¹⁺ decrease during the initial phase of inter-ELM, then increases with the duration of the inter-ELM. From t=6.0 s to t=7.8 s

(covering 18 ELM events), the total Mo radiation significantly decreases, indicating effective expulsion of Mo impurity ions with ELM bursts. In contrast, the W emission intensity in Fig. 6 fluctuates during t=6.0-7.4 s, but the baseline remains stable ($C_W \sim 1.6 \times 10^{-4}$). This difference is attributed to Mo impurity bursts at t=5.55 s and t=5.95s, which lead to a substantial transport of Mo impurities into the plasma core. In addition, based on the evolution of Mo and W impurity ions with multiple ionization states, it is confirmed that bursts of W and Mo sputtering events occurred during the time periods represented by the cyan and green shaded areas in Figs. 3, 5, and 6. A detailed analysis is provided in Fig. 7.

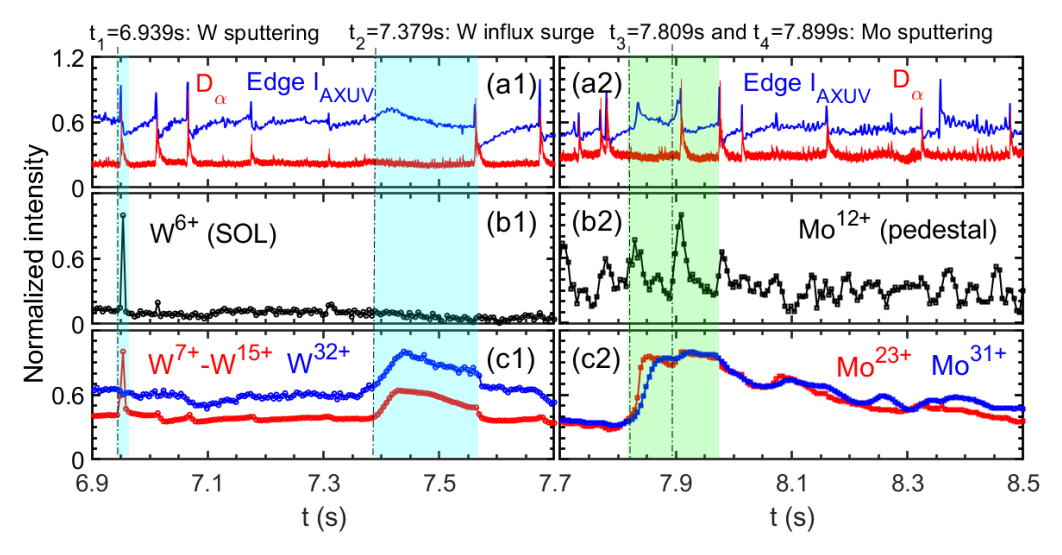


Fig. 7. Time evolutions of normalized emission intensity: (a1) and (a2) D_{α} intensity and Edge AXUV intensity, (b1) and (b2) W^{6+} and Mo^{12+} , (c1) W^{7+} - W^{15+} and W^{32+} , and (c2) Mo^{23+} and Mo^{31+} .

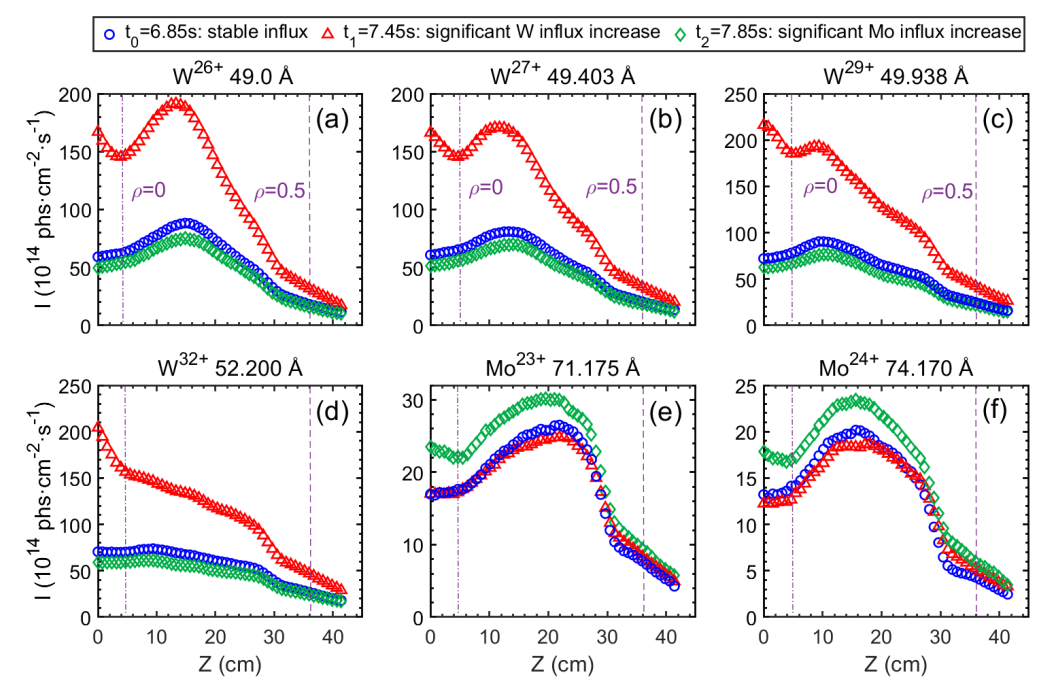


Fig. 8. Vertical intensity profiles of tungsten and molybdenum impurity ions measured by EUV_Long2_u spectrometer in EAST discharges #152527: (a) W^{26+} 49.0 Å, (b) W^{27+} 49.403 Å, (c) W^{29+} 49.938 Å, (d) W^{32+} 52.20 Å, (e) M^{o}^{23+} 71.175 Å, and (f) M^{o}^{24+} 74.170 Å observed at three timings: t_0 =6.85 s, t_1 =7.45 s, and t_2 =7.85 s.

Two W and two Mo impurity sputtering events demonstrate that type-I ELMevents effectively expel high-Z impurities from the main confinement region while preventing core penetration, helping maintain the high confinement steady-state plasma. As shown in Figs. 7(a1)-(c1), the first W sputtering event at t=6.939 s shows W⁶⁺ and W⁷⁺-W¹⁵⁺ emission increases but W³²⁺ decrease, confirming ELM-induced impurity expulsion despite transport to the pedestal. The second W sputtering event at

t=7.379 s exhibits similar W⁷⁺-W¹⁵⁺ and W³²⁺ evolution (t=7.418-7.576 s), resulting in significant energy loss (see Fig. 3(c)) until ELM clearance at t=7.567 s. Notably, absent W⁶⁺ and visible camera signatures suggest diagnostic viewing geometry effects, with EUV Long c (F-port) and visible camera (C-H ports) capturing different spatial regions. Figs. 7(a2)-(c2) show two Mo sputtering events that further corroborate these findings. The first event at t=7.809 s shows a significant increase in Mo radiation in both the pedestal and the core regions, demonstrating impurity penetration. The second event at t=7.899 s is characterized by extremely intense Mo¹²⁺ emission. An ELM burst 0.005 s later effectively prevents most impurities from penetrating the main confinement region. These observations indicate that multiple successive ELMs are required for complete impurity expulsion. Both Mo sputtering events originate near the low-field-side midplane, where transport into the plasma core is particularly efficient and can significantly increase central impurity concentrations. These results are consistent with observations on other tokamak devices. In addition, Fig. 8 shows vertical intensity profiles of Mo and W ions in the main confinement region at three characteristic times, i.e., t_0 =6.85 s for steady state without impurity influx surges, t₁=7.45 s with enhanced W influx, and t₂=7.85 s with enhanced Mo influx. The magnetic axis is at Z≈4.2 cm. During steady-state operation, profiles of W²⁶⁺-W²⁹⁺ and Mo²³⁺-Mo²⁴⁺ are clearly off-axis and hollow, indicating no core accumulation of high-Z impurities, even at C_W≈1.6×10⁻⁴. This behavior is consistent with on-axis ECRH enhancing core turbulent transport and suppressing impurity accumulation. Although increased W or Mo influx enhances radiation power, the maintained hollow profiles demonstrate that sputtering events enhance core radiation power without significantly altering high-Z impurity transport.

Based on experimental observations of impurity ions in the SOL-pedestal-core regions, the impurity transport process during type-I ELM cycles without sputtering events is as follows. During the intra-ELM phase, impurity ions near the pedestal are transported radially into the SOL and then rapidly reach the divertor target through parallel conduction along open field lines. This process significantly enhances recycling throughout the divertor. The recycled impurity ions are subsequently transported back toward the core region. After the ELM event ends, the reduced recycling source allows the impurity density in the SOL to recover to its initial level. Meanwhile, the impurity density from the pedestal to the core region then continues to increase slowly throughout the intra-ELM phase as impurity confinement continues to improve in this region [24]. However, due to the line-integral nature of the EUV spectrometer measurements in EAST, it is difficult to unambiguously resolve the detailed evolution process of impurity ions across the region from the pedestal foot to the SOL during the ELM cycle.

3. SUMMARY

A systematic analysis of tungsten impurity transport from the SOL to the main confinement region under different ELM regimes is presented for EAST and provides an experimental basis for impurity control and the sustainment of steady high-confinement plasmas. In NBI-dominated discharges, the core W concentration is 5.7×10^{-5} to 2.0×10^{-4} during type-I ELMs, and 5.6×10^{-6} to 6.3×10^{-5} during type-III ELMs. When type-III ELMs occur within the inter-ELM interval of type-I discharges, the core W concentration is dominated by these events. For type-I discharges, inter-ELM emission intensities of core W and Mo increase when $f_{ELM} < 7$ Hz. In addition, during the intra-ELM phase, impurity expulsion limits penetration of wall-sputtered species and reduces impurity content in the pedestal and the main confinement region. During the inter-ELM phase, improved confinement and SOL backflow, together with sputtering from the high- and low-field sides, facilitate impurity entry and enhance the core W concentration. Consequently, increasing f_{ELM} enhances intra-ELM expulsion relative to inter-ELM backflow and is expected to lower core high-Z impurity concentration.

ACKNOWLEDGEMENTS

This work was supported by the National MCF Energy R&D Program (Grant Nos. 2022YFE03180400, 2024YFE03000200, 2024YFE03000203), Chinese Academy of Sciences President's International Fellowship Initiative (PIFI) (Grant Nos. 2025PVA0060, 2024PVA0074), and National Natural Science Foundation of China (Grant No. 12322512). We thank all staff members at EAST (https://cstr.cn/31130.02. EAST), for providing technical support and assistance in data collections and analyses.

REFERENCES

- [1] Loarte A., et al., The new ITER baseline, research plan and open R&D issues, Plasma Phys. Control. Fusion 67 (2025) 065023.
- [2] Hu A.L., et al., A space-resolved visible spectrometer system using compact endoscopic optics for full vertical profile measurement of impurity line emissions in superconducting EAST tokamak, Journal of Instrumentation 20 (2025) C07022.
- [3] Ma J.Y. et al., First observation of full radial profile of Zeff using a high-performance visible spectrometer in EAST tokamak with full tungsten divertors, Journal of Instrumentation 20 (2025) C07016.
- [4] Zhang L., et al., A fast-time-response extreme ultraviolet spectrometer for measurement of impurity line emissions in the Experimental Advanced Superconducting Tokamak, Rev. Sci. Instrum. 86 (2015) 123509.
- [5] Xu Z., et al., An extreme ultraviolet spectrometer working at 10–130 Å for tungsten spectra observation with high spectral resolution and fast-time response in Experimental Advanced Superconducting Tokamak, Nuclear Inst. and Methods in Physics Research, A 1010 (2021) 165545.
- [6] Zhang L., et al., A space-resolved extreme ultraviolet spectrometer for radial profile measurement of tungsten ions in the Experimental Advanced Superconducting Tokamak, Nuclear Inst. and Methods in Physics Research, A. 916 (2019) 169-178.
- [7] Cheng Y.X., et al., Performance improvement of space-resolved extreme ultraviolet spectrometer by use of complementary metal-oxide semiconductor detectors at the Experimental Advanced Superconducting Tokamak, Rev. Sci. Instrum. 93 (2022) 123501.
- [8] Zhang W.M., et al., Spectroscopic analysis of tungsten spectra in extreme-ultraviolet range of 10-480 Å observed from EAST tokamak with full tungsten divertor, Phys. Scr. 99 (2024) 105609.
- [9] Zhang W. M., et al., Line identification of extreme ultraviolet (EUV) spectra from iron, copper and molybdenum ions in EAST tokamak, Phys. Scr. 97 (2022) 045604.
- [10] Li L., et al., Line identification of extreme ultraviolet (EUV) spectra from low-Z impurity ions in EAST tokamak plasmas, Plasma Sci. Technol. 23 (2021) 075102.
- [11] Li Z.W., et al., Machine learning application to wavelength calibration for Extreme Ultraviolet (EUV) spectroscopy in EAST tokamak, Journal of Instrumentation 20 (2025) C07002.
- [12] Shi S.Y., et al., Illustrating the physics of core tungsten (W) transport in a long-pulse steady-state H-mode discharge on EAST, Nucl. Fusion 62 (2022) 066040.
- [13] Shi S.Y., et al., Understanding core heavy impurity transport in a hybrid discharge on EAST, Nucl. Fusion 62 (2022) 066032.
- [14] Shi S.Y., et al., Understanding core tungsten (W) transport and control in an improved high-performance fully noninductive discharge on EAST, Nucl. Fusion 62 (2022) 066031.
- [15] Cheng Y. X., et al., Effect of 4.6 GHz LHW on tungsten transport in NBI dominant H-mode plasma, Nucl. Fusion 65 (2025) 062003.
- [16] Zhou Z., et al., Tungsten impurity reduction by ICRH in a high-power injection and high-performance H-mode discharge on EAST, Nucl. Fusion 65 (2025) 036004.
- [17] Fajardo D., et al., Integrated modelling of tungsten accumulation control with wave heating: validation in ASDEX Upgrade and predictions for ITER, Nucl. Fusion 64 (2024) 104001.
- [18] Zhou C.X., et al., The transport and radiation loss of tungsten impurities in core plasma for the CFEDR conventional H-mode scenario, Plasma Sci. Technol. 27 (2025) 104008.
- [19] Zhang F.L., et al., Evaluation of tungsten influx rate using line emissions from W⁵⁺ ions in EAST tokamak, Nucl. Fusion 65 (2025) 036037.
- [20] Zhang W.M., et al., First observation of edge impurity behavior with n=1 RMP application in EAST L-mode plasma, Nucl. Fusion 64 (2024) 086004.
- [21] Zhang W.M., et al., Effective control of intrinsic impurities using n = 1 resonant magnetic perturbation (RMP) in EAST H-mode plasma, Nucl. Mater. Energy 41 (2024) 101822.
- [22] Zhang W.M., et al., Edge and core impurity behavior and transport in EAST H-mode plasma with internal transport barrier, Nucl. Fusion 65 (2025) 052003.
- [23] Fajardo D. et al., Theory-based integrated modelling of tungsten transport in ITER plasmas, Plasma Phys. Control. Fusion 67 (2025) 015020.
- [24] Wade M.R., et al., Direct measurement of the impurity dynamics during an ELM cycle, Journal of Nuclear Materials 337-339 (2005) 737-741.